GSI

Preprint 2000 - 25
September

# Treatment planning for heavy ion radiotherapy: physical beam model and dose optimization

M. Krämer, O. Jäkel, T. Haberer, G. Kraft, D. Schardt, U. Weber



Gesellschaft für Schwerionenforschung mbH
Planckstraße 1 • D-64291 Darmstadt • Germany
Postfach 11 05 52 • D-64220 Darmstadt • Germany

# Treatment planning for heavy ion radiotherapy: physical beam model and dose optimization

**M Krämer†§, O Jäkel‡, T Haberer†, G Kraft†, D Schardt†, U Weber†**

†GSI Biophysik, Planck-Str. 1, D-64291 Darmstadt, Germany
‡DKFZ Heidelberg, INF 280, D-69120 Heidelberg, Germany

**Abstract.** We describe a novel code system, TRiP, dedicated to the planning of radiotherapy with energetic ions, in particular $^{12}C$. The software is designed to cooperate with three-dimensional active dose shaping devices like the GSI raster scan system. This unique beam delivery system allows to select any combination from a list of 253 individual beam energies, 7 different beam spot sizes and 15 intensity levels. The software includes a beam model adapted to and verified for carbon ions. Inverse planning techniques are implemented in order to obtain a uniform target dose distribution from clinical input data, i.e. CT images and patient contours. This implies the automatic generation of intensity modulated fields of heavy ions with as many as 40000 raster points, where each point corresponds to a specific beam position, energy and particle fluence. This set of data is directly passed to the beam delivery and control system. The treatment planning code is in clinical use since the start of the GSI pilot project in december 1997. To this end 48 patients have been successfully planned and treated.

§ To whom correspondence should be addressed.

## 1. Introduction

One of the main objectives in radiotherapy is the conformal delivery of the prescribed dose to the target volume, whereas the surrounding healthy tissue and critical structures should be spared as much as possible. In comparison with conventional photon beams, therapeutic ion beams in general offer the advantage of a depth dose distribution with a pronounced maximum (Bragg maximum) and a sharp dose fall-off at large penetration depth, in contrast to the exponential dose deposition of photons or neutrons, or the broad maximum generated by electrons. This is also known as *inverted dose profile* and it allows a higher degree of dose conformation to the target volume. Heavier ions like $^{12}C$ offer further advantages over protons or other lighter charged particles: First, the lateral scattering in tissue is reduced roughly by a factor of 3. This factor arises from Highland's parametrization of Moliere's scattering (Highland, 1975, 1979), where the projectile's charge $Z$ and momentum $p$ enter as $Z/\beta pc$ in the width of a gaussian distribution of scattering angles. Second, carbon ions have an increased relative biological effectiveness (RBE), especially in the stopping region at the Bragg peak. These particular properties make carbon ion beams an ideal candidate to be combined with the evolving techniques of intensity modulated radiotherapy (IMRT).

### *1.1. Dose shaping techniques*

Many radiotherapy facilities around the world already exploit the advantages of the inverted dose profile of heavy charged particles such as protons or carbon ions. Pioneering work was done at the LBL 1975-1993. They used a broad beam with a defined spread out Bragg peak generated by modulator wheels (ridge filters) (Chu *et al* , 1993). The field is shaped by patient specific passive devices like collimators to match the tumor in beams eye view and by compensators to match in longitudinal direction. With a fixed modulation for the spread out Bragg peak over the whole field, however, the dose cannot be tailored to the proximal end of the target volume, so that substantial dose is delivered to the adjacent normal tissue. Figure 1 shows a typical bolus used for broad beam techniques to compensate for the curvature of the target and the outer contour and illustrates its effect on the dose distribution. Similar techniques are used at NIRS (Kanai *et al* , 1999), the only other facility besides GSI which currently uses carbon ion beams for tumor therapy.

The next step to better exploit the advantages of ion beams are the various techniques of active volume scanning. They use magnetic deflection of narrow pencil-like beams to cover the cross sections of the target volume. Energy variation of the ion beams allows coverage of different slices at different depths (Figure 2). This results in an excellent dose conformation not only at the distal, but also at the proximal end of the target volume. So far two facilities have implemented this method for clinical use: PSI with the spot scanning technique for protons (Pedroni *et al* , 1995) and GSI with the raster scan device for ions. In contrast to GSI, PSI uses range shifters to adjust the particle energy and a one-dimensional beam scanning in combination with a linear

motion of the treatment table in the second dimension.

### *1.2. Heavy ion radiotherapy at GSI*

In december 1997 an experimental heavy ion radiotherapy facility became operational at the German heavy ion research center GSI (Gesellschaft für Schwerionenforschung, Darmstadt). The rationale for the use of heavy ions is that they combine a high degree of dose conformation, better than proton beams, with a high biological effectiveness focussed to the target volume. The clinical part of this pilot project will last for five years, using exclusively beams of $^{12}C$ ions. The aim is to investigate the clinical impact of the unique properties of heavy ions and to show which patients can benefit from such a therapy.

The GSI facility realizes for the first time a combination of an active field shaping, using a scanned beam, with an active energy variation of the beam, thus making full use of the advantages of heavy charged particles for therapy. The use of a magnetic scanning system (Haberer *et al* , 1993) together with the active energy variation allows irradiation with a very high degree of target conformality. This novel irradiation technique requires a method for dose calculation and optimization which is radically different from conventional approaches used for example in photon and even proton therapy, due to the strong dependence of the RBE on particle charge, energy and absorbed dose. A prerequisite is the development of a physical beam model as well as a radiobiological model to describe the interactions of ion beams with biological material.

The large number of different beam positions and intensities both in lateral as well as in longitudinal directions allow a high flexibility in volume scanning. This unique GSI system, therefore, comprises a fully threedimensional intensity modulation combined with high spatial resolution. Thus the precise computer-based planning of the beam energy and particle fluence is mandatory. The PSI spot scanning technique represents a similar system, however, with poorer spatial resolution due to their relatively large beam spot size.

For photon beams computer-based planning is common practice in radiotherapy and numerous commercial and research prototype packages exist. Whereas commercial packages offer mature solutions research prototypes have the advantage that they are more flexible in an experimental situation like the GSI radiotherapy. For heavy ions commercial treatment planning systems do not exist.

At the German Cancer Research Center DKFZ (Deutsches Krebsforschungszentrum, Heidelberg) a universal environment for radiotherapy planning in research and routine environments, Voxelplan, has been developed (Gademann *et al* , 1993). Although Voxelplan is very flexible as far as the selection of dose algorithms and beam delivery systems are concerned, its main application has been in high precision conventional therapy.

At other sites where charged particles are in use for radiotherapy, treatment

planning systems have been developed. However, all of them appear to be tailored to the specific needs of the respective facility. Early solutions for heavy ions like at the LBL (Chen *et al* , 1979) and current systems like the HIPLAN at NIRS (Endo *et al* , 1996) are designed for passive beam shaping only. The closest approach is found at PSI , however, their spot scanning system differs from GSI's scanning system and uses the absorbed dose of protons only. Hence, the specific properties of carbon ions like projectile fragmentation and the RBE variation with energy are not included.

None of these systems is directly well-suited to the specific needs of highly tumor conform treatment with ion beams, that is the unique combination of scanned beam and active energy variation, which leads to many thousands of free parameters to be determined. Due to the high RBE of heavy ions - which depends on location and absorbed dose - it is mandatory to perform treatment planning based on biological effectiveness. This cannot be done by applying some quality factor after the optimization: due to the complex non-linear nature of biological effectiveness, i.e. its dependence on particle charge and energy, absorbed dose and tissue type, it has to be an integral part of the treatment planning kernel.

In this article we describe the basic principles of the newly developed GSI computer code TRiP (**TR**eatment planning for **P**articles), which fulfills all the above requirements. In combination with Voxelplan as well as stand alone it serves as the standard treatment planning system for the GSI radiotherapy project since 1995. It is used on a regular basis for patient treatment as well as for irradiations of biological samples, phantoms and detectors for research purposes.

This article is organized as follows: section 2 describes the setup of the GSI beam delivery. This defines the requirements for the treatment planning which are summarized in section 3. Section 4 presents the physical beam model which has been incorporated as an integral part of the treatment planning and section 5 addresses the problem of tissue inhomogeneities. Section 6 describes the methods of dose calculation and optimization and finally some typical planning results are shown.

Two important aspects are not addressed here but will be the subject of separate forthcoming papers. These are the radiobiological aspects of treatment planning and the implementation of the system in clinical practice.

## 2. The GSI beam delivery system

This section describes in short the beam delivery system for the radiotherapy at GSI. The general design idea is to use completely active volume scanning in three dimensions. This can be achieved by magnetic deflection of the $^{12}C$ beam in lateral direction and by energy variation of the GSI synchrotron to cover different depths in order to spread out the dose across the target volume. Figure 2 shows a schematic overview.

GSI's SIS accelerator provides heavy ion beams from protons to Uranium with energies up to 2 GeV/u for lighter ions ($\approx$ 1 GeV/u for Uranium). For radiotherapy only light ions like carbon are used because they offer the best combination of RBE and

physical dose shaping.

In order to match the needs of radiotherapy the accelerator control system was modified to allow selection of the energy, beam spot size and intensity level of the $^{12}C$ beam from one synchrotron cycle to the next (Eickhoff *et al* 1996).

A list of 253 energies has been setup in order to achieve a constant spacing of the corresponding ranges in water. This is important to obtain a homogenous depth dose distribution. The energy range is between 80 MeV/u and 430 MeV/u corresponding to a range in tissue between 20 mm and 330 mm, respectively. The ion energy can be switched within $\approx$ 5 seconds and thus different depths can be reached without the need of additional absorbers. This way the target region is divided into subsequent slices corresponding to beams of different energies.

The nominal beam spot diameter can be chosen from a predefined list. Narrow beams are used for small volumes and in situations where sharp dose gradients at the field boundary are required. Larger beam spots are preferred for large target volumes because they reduce the number of scanning steps needed to cover such volumes. In practice, however, the size of the beam spot depends on the selected beam energy (Figure 3). For low beam energies this is due to multiple scattering in the beam exit window and the ionization and multiwire chambers of the beam control system. Although multiple scattering in general plays only a minor role for projectiles as heavy as $^{12}C$, the long travelling distance of about 1 meter between the beam outlet and the isocentre results in an enlarged beam spot. The beam profile is approximately symmetric and gaussian-shaped. The most common spot size setting is 5 to 6 mm FWHM, yielding a lateral dose fall-off (from 90% to 10%) of the same magnitude.

The magnetic scanning system (Haberer *et al* , 1993) deflects the ion beam in lateral (x,y) direction across a maximum field size of 200×200 mm. The main input to the control system are the particle fluences $F(E_{beam},x,y)$ determined by the treatment planning procedures as described later. Monitoring the prescribed dose thus is equivalent to monitoring the correct deliverance of the number of ions for each energy and position. This is achieved by a set of transmission ionization chambers (ICs), thereby compensating for very large fluctuations in beam flux (Voss *et al* , 1998). The ICs are calibrated against a standard dosimeter every morning as part of the daily checks. The computer control system is designed for a grand total number of 524288 irradiation positions. Irradiation times for typical cases are in the order of a few minutes. Large tumours of some hundred cubic centimeters in volume may require about 20 minutes of treatment time.

Due to space limitations and also for economic reasons no gantry is available, only a fixed horizontal beam line. However, the patient couch can be rotated, so that multi-field irradiation is possible at least in a single plane. At present most patients are treated with two approximately opposing fields. In some cases a third boost or a patch field of a different angle is superimposed.

## 3. Requirements for treatment planning

Treatment planning for scanned heavy ion beams starts just like conventional planning, that is, imaging devices such as magnetic resonance (MR) and computer tomography (CT) are used to generate a digital model of the irradiation region. While MR images deliver high resolution information on tumour location and critical structures, the CT data are mandatory for dose computation and optimization. CT data - taken without contrast drugs - essentially represent the density of electrons in tissue, and it is the electron density which determines the ion stopping power and hence the dose deposition as well as the particle ranges. We emphasize here that a CT taken with contrast agent should not be used for particle dose calculations because this would lead to erroneous particle ranges with deviations up to 2-3 mm. Based on the image data patient contours for the target volume and the critical structure are defined by means of a dedicated software package.

Beyond this point the treatment planning for $^{12}C$ ions has to account firstly for the specific properties of the ion species (in contrast to protons or photons) and secondly for the unique capabilities of GSI's irradiation facility. An additional requirement is that all algorithms and models developed for the absorbed dose calculation must be compatible with treatment planning based on the RBE.

The first requirement makes it necessary to describe the transport of $^{12}C$ ions in tissue in a way suitable for fast treatment planning. This rules out Monte Carlo (MC) techniques which are popular in other areas of physics. Moreover, methods developed for protons are not necessarily well suited due to $^{12}C$ specific features like projectile fragmentation and reduced lateral scattering of the beam.

The second requirement forces the implementation of "inverse" planning techniques. That is, the particle fluence is determined from the desired dose distribution by some optimization procedure. However, whereas in photon therapy only a few irradiation fields have to be considered, the GSI scanning system requires several thousands to tens of thousands of single scanner positions to be determined in order to obtain a uniform dose distribution across the target volume. E.g., the irradiation of an average target of 6 cm diameter (volume $\approx$ 110 $cm^3$) with scanner spots of 2 mm spacing and a Bragg peak distance of 2 mm in longitudinal direction will require the determination of fluence values at $\approx$ 14000 positions.

The raster scan technique implies that each slice of the target is irradiated with a non-uniform particle fluence distribution. Only the distal slice receives a homogeneous distribution of high particle fluences (Figure 4). All other slices are - dependent on geometry - partially pre-irradiated and hence require less dose and irregular dose patterns to be deposited. In particular, the requirements for heavy ion treatment planning can be listed as follows:

- A physical beam model has to be established which describes the ion interaction with tissue with sufficient accuracy. Such a model should be able to calculate the distribution of primary and secondary particles and their energies as a function of

depth. This is important because the interaction of heavy charged particles with biological structures such as the cell nucleus depends heavily on particle charge and energy. From the particle distribution the depth dose distribution for any desired beam energy is derived by multiplication with the energy loss.

- Algorithms have to be developed which are able to derive the particle energies and fluences from a prescribed dose distribution, not just calculate the absorbed dose straightforward from given particle fluences. This is known as *inverse* planning and is a very complex task in view of the many free parameters of the GSI scanning system.
- The relation of particle ranges to CT numbers has to be established. In general the patient tissue is inhomogeneous, that is, it comprises regions of various densities like water, bone, muscle, fat, air cavities and so on. Particle energy calculations have to account for such heterogeneities. Basically, methods have to be established to translate the CT information (representing x-ray attenuation) into a water equivalent path length relevant for heavy ions.

Apart from these overall requirements the planning of an actual patient irradiation comprises several output tasks:

- compute and store the absorbed dose distribution in three dimensions, either in the CT or in the water-equivalent coordinate system (to allow fast control of the optimization results),
- generate the input data for the magnetic beam scanning system and the SIS accelerator,
- support recalculation of dose distributions from externally supplied particle fluences (to allow phantom irradiation with patient plans),
- compute and store the expected read-outs of various dosimeters like TLD, films and others, which are supposed to have nonlinear dose response functions.

## 4. The beam model

The beam model we use so far is based on the fact that for ion beams as heavy as $^{12}C$ the multiple elastic scattering plays only a minor role (Figure 5). The light fragments, which are generated while a heavy ion traverses matter, will experience larger deflections. However, since they contribute only a small amount to the overall dose, their multiple scattering is neglected as well in first order. Future versions of the model will also include angular scattering of the generated light fragments. Likewise, all other particles which might be generated during $^{12}C$ slowing down such as $\gamma-$rays and $\delta-$rays are neglected because they contribute only negligibly to the dose (compared with the primary $^{12}C$) or because they are already included in the energy loss (low energy $\delta$ electrons).

Under these assumptions the (partial) dose generated by a single heavy ion beam with energy $E_{\text{beam}}$ centered at $(x_0, y_0)$ can be described as

$$D(E_{\text{beam}}, \boldsymbol{x}))[\text{Gy}] = 1.6 \times 10^{-8} \times d(E_{\text{beam}}, z)[\frac{\text{MeV}}{\text{gcm}^{-2}}] \times \frac{N}{2\pi\sigma^2[\text{mm}^2]} \exp(-\frac{1}{2}\frac{r^2}{\sigma^2}) \qquad (1)$$

where $r$ is the distance from the beam centre, $\sigma$ is the actual width (variance) of the Gaussian beam profile and $N$ is the total number of particles. The lateral beam profile is assumed to be gaussian in shape and symmetric in x and y. The most important quantity, however, is the energy loss distribution $d(E_{\text{beam}}, z)$, for a given initial beam energy, $E_{\text{beam}}$, as a function of penetration depth, $z$, which has to be described by an appropriate model. Such a model has to include not only the single particle energy loss, but also the energy loss straggling and the process of projectile fragmentation in order to reproduce experimentally determined dose profiles with sufficient accuracy.

We developed a code tailored to our needs (Haberer 1994), with as much experimental data incorporated as possible. Although focused on and tested for $^{12}$C ions it can be extended to other ion species as well. The basic concepts are described in the following.

### *4.1. The YIELD transport model*

The most important input to the dose calculation is the distribution $d(E_{\text{beam}}, z)$ generated by a heavy ion beam of energy $E_{\text{beam}}$ in water or water-equivalent material at depth $z$. Due to energy loss straggling and because heavy particles (compared to protons) undergo projectile fragmentation when travelling through matter the depth dose profile is different from the $\mathrm{d}E/\mathrm{d}x$ curve for a single particle. Target fragmentation occurs too, it is, however, of minor importance compared to projectile fragmentation. Our model is restricted to the description of the one-dimensional transport of the primary beam and the generated secondary particles. This task can be solved even without MC methods, which in this case is an advantage because $d(E_{\text{beam}}, z)$ is obtained without statistical fluctuations.

The absorber under consideration (water as a tissue equivalent) is divided into approximately 80 slices with thicknesses varying from 0.05 to 0.0005 times the expected Bragg peak position. With such an adaptive grid the rapid changes in the vicinity of the Bragg peak can be described without wasting computer resources in the entrance region where the radiation field changes only slowly with depth $z$. For each slice energy spectra $\mathrm{d}N(E_{\text{beam}}, z, T, E)/\mathrm{d}E$ for in-going (index $I$) and out-going (index $F$) particles are defined, where $T$ represents a particular particle species $(Z, A)$ defined by the nuclear charge $Z$ and the mass number $A$. Within each of these material slices of varying thickness $\Delta z_i$ new particles can be created by fragmentation of the ingoing ones:

$$\frac{\mathrm{d}N_{\text{F}}}{\mathrm{d}E_{\text{F}}}(T_{\text{F}}, E_{\text{F}}) = \sum_{T_{\text{I}}, E_{\text{I}}} \frac{\mathrm{d}N_{\text{I}}}{\mathrm{d}E_{\text{I}}}(T_{\text{I}}, E_{\text{I}})(1 - \exp(-\Delta z \sigma_{\text{I}\to\text{F}}(T_{\text{I}}, E_{\text{I}}) n_{\text{nuclei}}))$$
$$\times \exp(-\frac{1}{2}\frac{(E_{\text{F}} - < E(E_{\text{I}}, E'_{\text{I}}) >)^2}{< \sigma^2(E_{\text{I}}, E'_{\text{I}}) >}) \qquad (2)$$

Here $\sigma_{I\to F}(T_I, E_I)$ is the cross section for the creation of a fragment species $T_F$ from its parent species $T_I$ by nuclear fragmentation reactions. It is derived from semi-empirical descriptions (Sümmerer *et al* 1990, Schall *et al* 1996). $n_{\text{nuclei}}$ is the number density of nuclei. The values in brackets, $< E >$ and $< \sigma^2 >$ are mean energy and mean energy variance after momentum loss by fragmentation, according to Morrissey (1989), with $E'_I = E_I - dE/dx(T_I, E_I)\Delta z$. The energy loss $dE/dx(T, E)$ is interpolated in well-established tables (Heinrich *et al* 1991). Simultaneously the ingoing particle spectrum is transformed by attenuation, energy loss and energy loss straggling:

$$\frac{\mathrm{d}N_F}{\mathrm{d}E_F}(T_F, E_F) = \sum_{E_I} \frac{dN_I}{dE_I}(T_I = T_F, E_I) \exp(-\Delta z \sigma_{\text{att}}(T_I, E_I) n_{\text{nuclei}}) \times \exp(-\frac{1}{2} \frac{(E_F - < E(E_I) >)^2}{< \sigma^2(E_I) >}) \quad (3)$$

Here $\sigma_{\text{att}}$ is the empirically corrected total reaction cross section. The values in brackets, $< E >$ and $< \sigma^2 >$ are mean energy and energy loss straggling, respectively, after electronic energy loss within the slice under consideration

After the calculation of one slice is completed the "outgoing" spectrum becomes the "ingoing" spectrum for the next slice. Finally the depth dose distribution is derived:

$$d(E_{\text{beam}}, z) = \sum_T \int_E \mathrm{d}E \frac{\mathrm{d}N}{\mathrm{d}E}(E_{\text{beam}}, z, T, E) \times \frac{\mathrm{d}E}{\rho \mathrm{d}x}(T, E) \quad (4)$$

The model calculations have been verified experimentally at several selected energies with large area ionization chambers and a precision water absorber of variable thickness (Sihver *et al* 1998). Figure 6 shows measured together with calculated depth dose distributions. Good agreement is achieved after slight adjustment of the energy loss table in order to reproduce the measured absolute Bragg peak position with sub-millimeter precision. The only adjustable parameter here is the ionization potential, $I_{\text{pot}}$, which enters into the usual stopping power formulae (Heinrich *et al* 1991, Salomon 1980). We found a value of $I_{\text{pot}} = 77$ eV is necessary to reproduce the measured Bragg peak positions. Increasing $I_{\text{pot}}$ by 2 eV shifts the peak position by $\approx 0.5$ mm for a $^{12}$C beam at 270 MeV/u. Our calculated Bragg peak positions are 8.35 and 14.49 g/cm$^2$ for 195 and 270 MeV/u, respectively, in good agreement with the experimental data of $8.34 \pm 0.04$ and $14.45 \pm 0.04$ g/cm$^2$.

At depth values beyond the Bragg peak the long range tails resulting from beam fragmentation contribute to the dose with a significant amount. These tails are reproduced by the model, too, and are also taken into account for the dose calculation and optimization.

For practical use in therapy planning it is sufficient to calculate the depth dose profiles in steps of 10 MeV/u initial beam energy from 50 to 500 MeV/u. The profiles are calculated only once and then stored as tables. The fragment spectra $\mathrm{d}N(E_{\text{beam}}, z, T, E)/\mathrm{d}E$ for each depth are stored as well, to be used in algorithms where the fragment and energy distribution is required, such as calculation of RBE or response of solid state detectors. When beam energies are required which are not represented

in the pre-calculated database, linear interpolation between the next neighbours is performed. This is facilitated if dose profiles and particle spectra are normalized prior to the actual interpolation, that is, the depth $z$ is normalized to the Bragg peak position (Figure 7 ) and the fragment energy, $E$, to the incoming beam energy, $E_{\mathrm{beam}}$.

### *4.2. The ripple filter*

At beam energies below about 150 MeV/u the unmodified Bragg peaks become very sharp ($\approx$ 1 mm FWHM in water at 100 MeV/u, $\approx$ 5 mm FWHM in water at 300 MeV/u), so that many energy slices would be needed to deliver a homogeneous dose distribution, thereby increasing the treatment time. An additional technical complication is caused by the scanner monitoring devices. Given a particular dose, there will be an increasing number of scanner positions with very small particle numbers as the number of slices grows. This would require a scan monitor system with a very high sensitivity for measuring the charge produced by low particle fluences as well as a high dynamic range. In order to circumvent this problem, we introduce the only passive (and static) beam shaping element, the so-called ripple filter. Its comb-like shape leads to a small but well defined broadening of the Bragg peak, especially for low beam energies (Weber and Kraft, 1999).

The transmission function of this device can be described as a set of different Bragg peak displacements, $\Delta z_i$, caused by the different traversal paths. They occur with different probabilities $w_i$, so that the transmission function can be folded with the basic data (depth dose profiles and spectral distributions) to obtain a modified set of basic data:

$$\begin{aligned} d'(E_{\mathrm{beam}}, z) &= \textstyle\sum_i d(E_{\mathrm{beam}}, z + \Delta z_i) w_i, \\ \tfrac{\mathrm{d}N'}{\mathrm{d}E}(E_{\mathrm{beam}}, z, Z, E) &= \textstyle\sum_i \tfrac{\mathrm{d}N}{\mathrm{d}E}(E_{\mathrm{beam}}, z + \Delta z_i, Z, E) w_i, \\ \textstyle\sum_i w_i &= 1 \end{aligned} \tag{5}$$

All dose and optimization algorithms remain unchanged, only the databases for the calculations are chosen differently with or without the ripple filter. We would like to emphasize at this point, that our ripple filter is no primary beam shaping device as described e.g. by Kanai *et al* (1999). Its main purpose is to broaden slightly the width of the sharp Bragg peaks of lower energies and thus to simplify the superposition of Bragg peaks.

## 5. Tissue inhomogeneities

The algorithms and procedures described so far are based on the assumption of water targets. However, biological tissues, e.g. lung and bone, have densities which differ considerably from that of water. The basic idea to account for such density variations is to apply the concept of a water-equivalent path length (WEPL) when an ion traverses

a CT voxel. High density voxels correspond to ion path lengths larger than that for water, low density voxels to shorter ion path lengths. In this way the trajectory of an ion through the CT cube is transformed from the CT system into a water-equivalent system in the beams-eye-view. Thus the originally regular shaped target volume will be distorted in the water-equivalent system (Figure 8) The advantage of this approach is twofold: The models as developed for water can be re-used without change and the anyway necessary coordinate system transformation between the CT system and the beams-eye-view can be incorporated into the calculational procedure as well.

The main problem is to establish the relation between the information given by the CT and the water-equivalent path length for ions, in particular carbon. There is no direct functional dependence between Hounsfield number and equivalent path lengths on the basis of a theoretical prescription. The Hounsfield numbers reflect the attenuation of x-rays, mainly by the photoelectric effect, whereas the ion path length is dominated by the ion energy loss processes. The actual chemical composition affects both quantitities but with different functional dependence on the atomic number $Z$ of the contributing atoms. Hence the desired relation cannot be retrieved from the knowledge of the CT number alone. However, a scatter plot of measured path length versus CT number reveals a piecewise linear relation at least for tissue equivalent materials. Due to the possibly different characteristics of the different x-ray tubes the relation between Hounsfield number and relative path length depends also on the type of CT device used. Our CT scanner is a Siemens Somatom Plus 4. Figure 9 shows earlier results from Minohara *et al* (1993) and Jacob (1996) who used phantom materials, together with recent measurements on animal tissue as reported by Geiss *et al* (1999). There is good agreement for large CT numbers. Deviations up to 20% exist predominantly in the low density region, corresponding to lung tissue.

The results of the phantom measurements can be represented as straight line segments, according to the results of Minohara *et al* (1993).

$$\mathrm{WEPL} = \begin{cases} 1.075 \times 10^{-3} \times \mathrm{CT} + 1.050, & \mathrm{CT} < -49 \\ 4.597 \times 10^{-4} \times \mathrm{CT} + 1.019, & \mathrm{CT} \geq -49 \end{cases} \tag{6}$$

and according to Jacob (1996)

$$\mathrm{WEPL} = \begin{cases} 1.011 \times 10^{-3} \times \mathrm{CT} + 1.052, & \mathrm{CT} < -60.81 \\ 4.190 \times 10^{-4} \times \mathrm{CT} + 1.016, & \mathrm{CT} \geq -60.81 \end{cases} \tag{7}$$

where $CT$ is the Hounsfield number. We have adopted the tissue results from Geiss *et al* (1999) as the best approach, shown as the solid line in Figure 9. In practice linear interpolation between the breakpoints is used to obtain path length values for any CT number. A similar representation was chosen by Schaffner *et al* (1998).

The actual algorithm of inhomogeneity correction proceeds as follows: First the intersections of the ion beam path at the different raster positions with the CT voxels

are calculated by solving the set of vector equations

$$\begin{aligned} \boldsymbol{x}_\mathrm{r} + \lambda_\mathrm{r}^{(x_i)} \boldsymbol{e}_\mathrm{beam} &= \boldsymbol{X}_\mathrm{CT}^{(i)} \\ \boldsymbol{x}_\mathrm{r} + \lambda_\mathrm{r}^{(y_i)} \boldsymbol{e}_\mathrm{beam} &= \boldsymbol{Y}_\mathrm{CT}^{(i)} \\ \boldsymbol{x}_\mathrm{r} + \lambda_\mathrm{r}^{(z_i)} \boldsymbol{e}_\mathrm{beam} &= \boldsymbol{Z}_\mathrm{CT}^{(i)} \end{aligned} \tag{8}$$

with respect to the $\lambda_\mathrm{r}$ where the $\boldsymbol{x}_\mathrm{r}$ are the raster positions, $\boldsymbol{e}_\mathrm{beam}$ is the unit direction vector of the beam and the $\boldsymbol{X}_\mathrm{CT}^{(i)}, \boldsymbol{Y}_\mathrm{CT}^{(i)}, \boldsymbol{Z}_\mathrm{CT}^{(i)}$ describe the x-, y- and z-planes of the CT grid. After rearranging for increasing values the $\lambda_\mathrm{r}$ describe the paths of the ions through the CT cube.

Then the water-equivalent path length for heavy ions is derived voxel by voxel by interpolation in the Hounsfield-range table. and applied as a correction factor for the $\lambda_\mathrm{r}$. In this way a look-up table between actual position within the CT voxel space and the position in the water-equivalent system can be established for each raster position. No corrections are applied in lateral directions, however. Another correction which has to be considered here is the material between the beam outlet and the patient, which is not part of the CT plan and hence is added as an extra water-equivalent offset. It is determined experimentally, its value is usually on the order of a few mm.

## 6. Calculation and optimization of physical dose

The algorithms described in this sections were selected under the assumption that only a single field (or beam port) has to be optimized at a time. This restriction is justified for our current irradiation facility where in most cases only two fields from two different directions are applied. Of course each field still comprises many different scanner positions and beam energies. Single field optimization allows various simplifications. The most important one is that the optimization, i.e. the determination of the particle numbers $N(E_\mathrm{beam}, x, y)$, can be performed in the water-equivalent system in beams-eye-view. This is an advantage because all databases are designed for water as target material. For the assessment of the quality of the whole treatment plan the final dose computation of course needs to be performed on the entire CT grid, using the particle numbers $N(E_\mathrm{beam}, x, y)$ resulting from the previous optimization step. These two major tasks are described in the following subsections.

### *6.1. Dose optimization*

For the dose optimization it is sufficient in first order to use one-dimensional dose distributions $d(E_\mathrm{beam}, z)$ because the lateral beam scattering is negligible compared to the initial beam width as delivered by the beam optics. In this case the dose computation (equation 1) can be simplified to

$$D(E_\mathrm{beam}, \boldsymbol{x})[\mathrm{Gy}] = 1.6 \times 10^{-8} \times d(E_\mathrm{beam}, z)[\frac{\mathrm{MeV}}{\mathrm{gcm}^{-2}}] \times F(E_\mathrm{beam}, x, y)[\mathrm{mm}^{-2}] \tag{9}$$

with the fluence

$$F(E_{\text{beam}}, x, y) = \frac{N(E_{\text{beam}}, x, y)}{\Delta x \Delta y} \tag{10}$$

where the $\Delta x$ and $\Delta y$ are the scanner step sizes in x and y, respectively. Within the target volume the lateral overlapping of neighbouring beam positions compensates for this crude approximation of a gaussian profile by a delta function. It has been shown (Haberer 1993, Weber 1996) that such an approximation is sufficiently accurate if the lateral scanning steps are chosen as a small fraction of the beam width

$$\Delta x = \Delta y \leq f_{\text{F}} \times \text{FWHM} \tag{11}$$

Empirically, we adopt a value of $f_{\text{F}} = 1/3$. Figure 10 illustrates that we achieve a sufficiently homogeneous dose with this choice. With the scanner positions chosen this way, the dose at each position is a superposition of many elementary beams

$$D(\boldsymbol{x}) = \sum_{E_{\text{beam}}} d(E_{\text{beam}}, \boldsymbol{x}). \tag{12}$$

Therefore the dose is nearly independent of the shape of the beam profile, which is another advantage of the scanning beam compared to volume shaping with absorbers.

For the GSI radiotherapy, dose optimization means finding an optimum set of accelerator energies, $E_{\text{beam}}$, to cover the whole depth range and for each energy and scanner position $(x, y)$ the corresponding particle numbers $N(E_{\text{beam}}, x, y)$ to achieve the prescribed dose. Of course the optimization algorithms must take into account the capabilities and restrictions of the irradiation system (accelerator, raster scanner, patient positioning system). The optimum set of data is determined in several steps. The starting point is a CT data cube together with the desired target volume, given as polygons within the different CT slices, and the prescribed dose. Then:

(i) If not yet done, the isocentre (reference point) is determined as the geometrical centre of gravity of all polygon contours defining the target region. The isocentre (in CT coordinates) coincides with the origin of the raster scanner system. The maximum lateral extension of the target region in beams eye view with respect to the isocentre is calculated. The scanner step size $\Delta x = \Delta y$ can be selected manually or is determined automatically from the desired nominal beam focus by (equation 11). This determines automatically the raster grid in x- and y-direction.

(ii) The trajectories of the ions at the scanner positions through the CT cube are determined and corrected for tissue inhomogeneities. From this information the extent of the target volume in beam direction and hence the minimum and maximum beam energies are determined. The actual energies are chosen in agreement with the table of energies available from the accelerator.

(iii) Once the beam energies are known, the desired nominal beam spot size is matched with the accelerator table. For each selected energy the next largest width is picked up from the table, in order to fulfill the homogeneity condition equation 11. If such a selection is not possible, the whole plan is rejected and a different spot size has to be used.

(iv) In order to account for the dose fall-off at the lateral edges of the target volume due to the finite beam width a "virtual contour extension" is performed. That is, within a lateral margin around the target volume in beams-eye-view additional scanner positions are adopted. The margin is defined as an adjustable fraction of the real beam width, usually 0.6 to 0.7. A contour extension in longitudinal direction does not appear necessary due to the much steeper dose fall-off in that direction.

The task of particle fluence optimization with respect to dose represents a least squares minimization with respect to the fluence values $F(E_{\text{beam}}, x, y)$:

$$\begin{aligned} &\chi^2 = \textstyle\sum_z w(\boldsymbol{x})(D_{\text{prescribed}} - D(\boldsymbol{x}))^2, \\ &\partial\chi^2/\partial F = 0. \end{aligned} \tag{13}$$

with appropriately chosen weight factors $w(\boldsymbol{x})$ and the dose $D(\boldsymbol{x})$ as given by equation 9. The prescribed dose $D_{\text{prescribed}}$ is assumed to be constant, but could in principle also depend on the location $\boldsymbol{x}$ within the CT. Because the parameters $F(E_{\text{beam}}, x, y)$ enter linearly into equations 9 and 13 the minimization problem could in principle be solved analytically. However, this is not a good solution in our case, due to the obvious constraint that there should be no negative fluence values. In fact, the threshold even is a small positive number because the intensity monitor of the scanner system requires a minimum number of particles to work correctly.

Furthermore, the algorithm should work also for cases where the optimization function depends nonlinearly on the optimization parameters. This is the case, for example, for the optimization based on the biologically equivalent dose, where the physical dose $D = D_{\text{phys}}$ is replaced by the biological one $D = D_{\text{bio}} = D_{\text{phys}} \times \text{RBE}(\text{d}N(E_{\text{beam}}, z, Z, E)/\text{d}E)$.

These requirements lead to the choice of iterative procedures, which are implemented in two steps:

(i) The single depth dose curves are directly matched slice by slice with the desired dose distribution. Figure 11 illustrates the principle of the algorithm. The procedure starts in the distal part of the target volume with the highest beam energy involved and proceeds to the proximal part. Dose contributions from the previous steps are taken into account. The whole procedure is repeated several times in order to account for the fragment tails beyond the Bragg peak. It gives already a very good approximation to the desired dose distribution. However, the algorithm matches only the peaks of the depth dose curves with the desired dose distribution. Because the overlapping of Bragg peaks is not always perfect, valleys may occur between the peaks, causing a systematic overall underdosage of a few percent. This can be corrected by subsequently applied minimization algorithms.

(ii) Starting with the preliminary $F(E_{\text{beam}}, x, y)$ obtained by the matching algorithm a true $\chi^2$-minimization is performed. Due to the similarity of the problem to the task of function fitting, text book algorithms like those described by Bevington

(1969) and Brand (1992) can be applied. In our case the fit function parameters correspond to the fluence values and the input data uncertainties to weight factors $w$ which are assumed to correspond to some constant fraction $f_w$ of the prescribed dose:

$$w = (f_w \times D_{\text{prescribed}})^{-2} = const. \tag{14}$$

$f_w$ can be varied but is chosen as 2.5% by default. This corresponds to an allowed uncertainty of 2.5% of the dose, in analogy to the way experimental uncertainties are accounted for in conventional function fitting. Additionally, reasonable uncertainties of the resulting fluences could be evaluated, just like the parameter uncertainties after function fitting.
The conjugate gradient as well as an adaption of Marquardt's algorithm has been implemented to solve equations 13. Marquardt's algorithm has the advantage that it converges reasonably also in the vicinity of the $\chi^2$-minimum, where the gradient is close to zero. Because the Marquardt algorithm evaluates curvature matrices it automatically offers means to derive an estimate of the fluence uncertainties, a feature which has, however, not been used so far. Conjugate gradients, on the other hand, allow the handling of huge parameter sets because they do not require the allocation, evaluation and inversion of large matrices. This is an advantage in view of the possibly thousands of adjustable fluence values we have to cope with.

Both steps account for the minimum particle limit by resetting the fluence value for a single position to zero if they fall below this limit. In such cases the neighbouring raster positions have to take over in order to fill the gap. Obviously this is possible only for a small number of such "omitted" positions and reasonably low minimum particle limit, otherwise it is impossible to obtain a homogeneous dose distribution.

### *6.2. Dose calculation on the CT grid*

After single field optimization in the water-equivalent system the dose distribution has to be calculated on the CT grid in order to be assessed. The dose calculation is based on the beam profile equation 1. CT voxel coordinates $\boldsymbol{x}_{\text{CT}}$ are transformed into their water-equivalent beams-eye-view system counterparts $\boldsymbol{x}_{\text{H2O}}$. Due to the regular and usually congruent raster coordinate grid the appropriate lower raster positions $(x_k, y_l)$ are rapidly located via binary grid search (figure 12). With the relative weighting factors $\xi_i$ according to the position of $\boldsymbol{x}_{\text{H2O}}$ within the raster grid

$$\begin{aligned}
\xi_1 &= (1-t)(1-u) \\
\xi_2 &= t(1-u) \\
\xi_3 &= (1-t)u \\
\xi_4 &= tu \\
t &= \frac{x-x_k}{x_{k+1}-x_k} \\
u &= \frac{y-y_l}{y_{l+1}-y_l}
\end{aligned} \tag{15}$$

bilinear interpolation is performed with contributions from all four neighbouring raster positions:

$$D(\boldsymbol{x}) = 1.602189 \times 10^{-8} \sum_{E_{\text{beam}}} \sum_{i=1}^{4} \xi_i d(E_{\text{beam}}, z_i) N_{\text{acc}}(E_{\text{beam}}, x_i, y_i) \qquad (16)$$

where the $d(E_{\text{beam}}, z_i)$ is obtained by linear interpolation in the depth dose database. The particle numbers, $N_{\text{acc}}(E_{\text{beam}}, x_i, y_i)$, of the four neighbouring positions themselves comprise accumulated contributions from all other raster positions $(x_j, y_j)$:

$$N_{\text{acc}}(E_{\text{beam}}, x_i, y_i) = \sum_j N(E_{\text{beam}}, x_j, y_j) \times \frac{1}{2\pi\sigma^2} \exp(-\frac{1}{2}\frac{r_{ij}^2}{\sigma^2}) \qquad (17)$$

with $r_{ij}^2 = (x_i - x_j)^2 + (y_i - y_j)^2$. Only contributions larger than 1% are taken into account for the accumulation, in order to reduce the number of correlation matrix elements represented by the exponential factor. To save computation time these matrix elements are precalculated once and stored for later use.

### *6.3. Optimization results*

Figure 13 shows the application of the described methods to a patient plan. Scanner step size was 2 mm and $^{12}$C energies were selected so that the distance between the Bragg peaks was $\approx$ 3 mm. These selections result in 39 energy slices with a total number of $\approx$ 10000 raster positions. A total number of $\approx 7 \times 10^8$ $^{12}$C ions are needed to deliver an absorbed dose of 1 Gy in the target volume ($\approx$ 120cm$^3$). The dose distribution conforms well to the target volume already with a single field (part (b)). Part (a) shows the dose profile on a line through the isocentre. The calculated dose follows closely the prescribed dose in the target region. It should be noted that for the same result without a ripple filter about 3 times as many energy slices and raster positions would be needed, with the same total number of particles.

## 7. Summary and Conclusion

We have developed the first therapy planning system which is able to generate a strictly tumour conformal irradiation using intensity modulated fields of heavy ions. It fully supports the raster scanning technique and the active energy variation of the GSI beam delivery system. Because it is designed for heavy ions, it includes the RBE in routine planning, which, however, will be addressed in a separate publication. These features make it a unique tool for the cancer treatment with heavy ions. The TRiP system standalone as well as in combination with Voxelplan is in use since 1995 for the planning of numerous irradiation experiments including inhomogeneous phantoms, cell and animal experiments such as mini-pig lungs and the central nervous system of rats. In addition, it is used to plan the irradiation of condensed phase detectors such as thermoluminescent detectors (TLDs) (Geiß *et al* , 1998) photographic film emulsions (Bathelt et al, 1998) and BANG gels (Ramm *et al* 2000). The response of these detectors

depends on charge and energy of the traversing ions and hence its prediction requires the knowledge of the charged particle field, similar to the calculation of the RBE.

So far 48 patients were treated at GSI since December 1997, using the treatment planning code as described in this paper.

Extensive quality assurance tests have been performed to ensure the validity of the dose calculation algorithm as well as the complete dose application system. A complete review of the results of these measurements will be given in a forthcoming publication.

Future developments will primarily be directed towards further exploitation of the unique characteristics of GSI's active volume shaping technique, in particular multiport treatments where the fields are optimized simultaneously. This would offer improved means to spare critical structures. The introduction of raster scanner grids with variable spacing or, ultimately, completely irregular grids would improve dose conformation close to steep lateral density gradients.

Efforts will also be devoted to a meaningful and realistic comparison of treatment plans for different beam modalities, such as protons, intensity modulated photon plans and $^{12}$C-plans generated at NIRS using compensators and ridge filters. Only such a comparison can show where the advantages of heavy ions versus other particles are and what benefit can be expected for the patient from the use of an active field shaping compared to the various passive field shaping techniques.

## References


Bathelt B, Krämer M, Scholz M and Kraft G 1998 Response of Photographic Emulsions to Ionizing Radiation *Max-Planck-Institut f. Kernphysik, Annual Report* (Heidelberg) p 214

Bevington Ph R 1969 *Data reduction and error analysis* (New York: McGraw Hill)

Brandt S 1992 *Datenanalyse* (Mannheim: BI-Wiss.-Verl.)

Chen G T Y, Singh R P, Castro J R, Lyman J T and Quivey J M 1979 Treatment planning for heavy ion radiotherapy *Int. J. Radiation Oncology Biol. Phys.* **5** 1809-1819.

Chu W T, Ludewigt B A and Renner T R 1993 Instrumentation for treatment of cancer using proton and light-ion beams *Rev. Sci. Instrum.* **64** 2055-2122.

Eickhoff T, Franczak B, Krause U, Riedel C, Rösch W, Steiner R 1996 Accelerator development for the GSI therapy project *GSI-report 96-01*

Endo M, Koyama-Ito H, Minohara S, Miyahara N, Tomura H, Kanai T, Kawachi K, Tsujii H and Morita K 1996 HIPLAN - a heavy ion treatment planning system at HIMAC *J. Jpn. Soc. Ther. Radiol. Oncol.* **8** 231-238.

Gademann G, Schlegel W, Bürkelbach J, Laier C, Behrens S, Brieger S, Wannenmacher M, 1993 Dreidimensionale Bestrahlungsplanung. Untersuchungen zur klinischen Integration, *Strahlentherapie und Onkologie* **169** 159-167.

Geiß O B, Krämer M and Kraft G 1998 Verification of Heavy Ion Dose Distributions Using Thermoluminescent Detectors. *Nucl. Instrum. Methods* **B146** 541-544

Geiß O B, Schardt D, Voss B, Krämer M and Kraft G 1999 Correlation between CT Number and Water Equivalent Thickness *GSI-report 99-01*

Haberer Th et al. 1993 Magnetic scanning system for heavy ion therapy, *Nucl. Instrum. Methods* **A330** 296-305.

Haberer T 1994 Entwicklung eines magnetischen Strahlführungssystems zur tumorkonformen Strahlentherapie mit schweren geladenen Teilchen, *GSI-report 94-09*

Heinrich W, Wiegel B amd Kraft G 1991 $\beta$, $Z_{eff}$, dE/dx, range and restricted energy loss energy loss of heavy ions in the region $1 \leq E \leq 1000$ MeV/u, *GSI-preprint 91-30*

Highland V L 1975 Some practical remarks on multiple scattering. *Nucl. Instrum. Methods* **129** 497-499 ——1979 **161** 171.

Jacob C 1996 Reichweite-CT-Zahl-Beziehung von Phantommaterialien und Messungen mit einer neuentwickelten multisegmentierten Ionisationskammer zur Dosisverifikation bei Schwerionenbestrahlung. *PhD thesis* (Heidelberg).

Kanai T, Endo M, Minohara S, Miyahara N, Koyama-Ito H 1999 Biophysical characteristics of HIMAC clinical irradiation system for heavy-ion radiation therapy. *Int. J. Radiation Oncology Biol. Phys.* **44** 201-210.

Minohara S, Kanai T, Endo M, Kawachi K 1993 Effects of object size on a function to convert x-ray CT numbers into the water equivalent path length of charged particle beams. *Proceedings of the Third Workshop on Physical and Biological Research with Heavy Ions* Ando K, Kanai T (eds.) (NIRS-M-99 HIMAC-006) p 14-15

Morissey D J 1989 Systematics of momentum distributions from reactions with relativistic ions *Phys. Rev.* **C39** 460-470

Pedroni E, Bacher R, Blattmann H, Böhringer T, Coray A et al. 1995 The 200-MeV proton therapy project at the Paul Scherrer Insitute: Conceptual design and practical realization. *Med. Phys.* **22** 37-53.

Ramm U, Weber U, Bock M, Krämer M, Bankamp A, Damrau M, Thilmann C, Böttcher H D, Schad L R, Kraft G 2000 Three-dimensional BANG Gel Dosimetry in Conformal Heavy Ion Radiotherapy. *Phys. Med. Biol. submitted.*

Salomon M H 1980 A Range-Energy Program for Relativistic Heavy Ions in the Region $1 < E < 3000$ MeV/amu *LBL Report 10446*

Schall I, Schardt D, Geissel H, Irnich H, Kankeleit E, Kraft G, Magel A, Mohar M F, Münzenberg G, Nickel F, Scheidenberger C, Schwab W 1996 Charge-changing nuclear reactions of relativistic light-ion beams ($5 \leq Z \leq 10$) passaging through thick absorbers, *Nucl. Instrum. Methods* **B117** 221-234.

Schaffner B and Pedroni E 1998 The precision of proton range calculations in proton radiotherapy treatment planning: experimental verification of the relation between CT-HU and proton stopping power *Phys. Med. Biol.* **43** 1579-1592

Sihver L, Schardt D and Kanai T 1998 Depth-Dose Distributions of High-Energy Carbon, Oxygen and Neon Beams in Water *Jpn. J. Med. Phys.* **18/1**

Sümmerer K, Brüchle W, Morissey D J, Schädel M, Szweryn B and Weifan Y 1990 Target fragmentation of Au and Th by 2.6 GeV protons *Phys. Rev.* **C42** 2546-2561

Voss B, Junk H, Stelzer H 1998 **ICs** The Monitor System of the Therapy Project *GSI-report 98-01*

Weber U 1996 Volumenkonforme Bestrahlung mit Kohlenstoff-Ionen zur Vorbereitung einer Strahlentherapie *Ph D Thesis Darmstadt*

Weber U and Kraft G 1999 Design and construction of a ripple filter for a smoothed depth dose distribution in conformal particle therapy *Phys. Med. Biol.* **44** 2765-2775

**Figures**

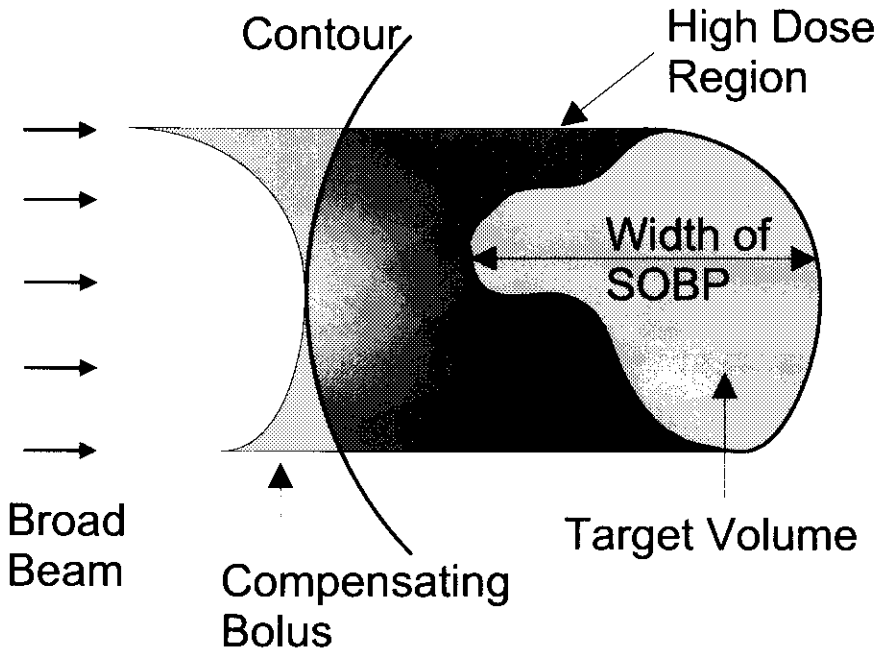


**Figure 1.** Passive shaping of a broad beam with a compensating bolus and its effect on the dose distribution.

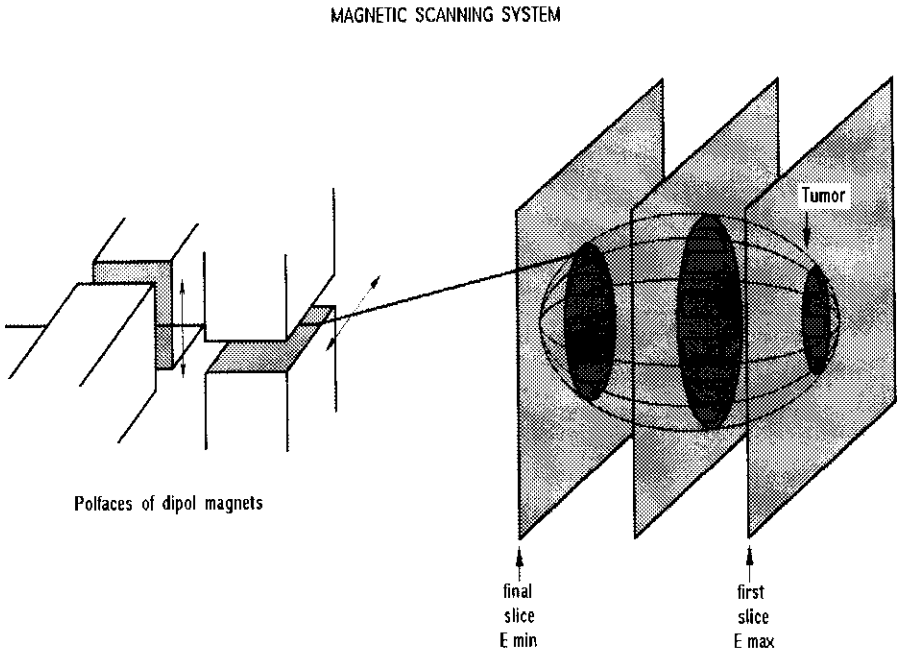


**Figure 2.** Schematic view of the magnetic scanning system.

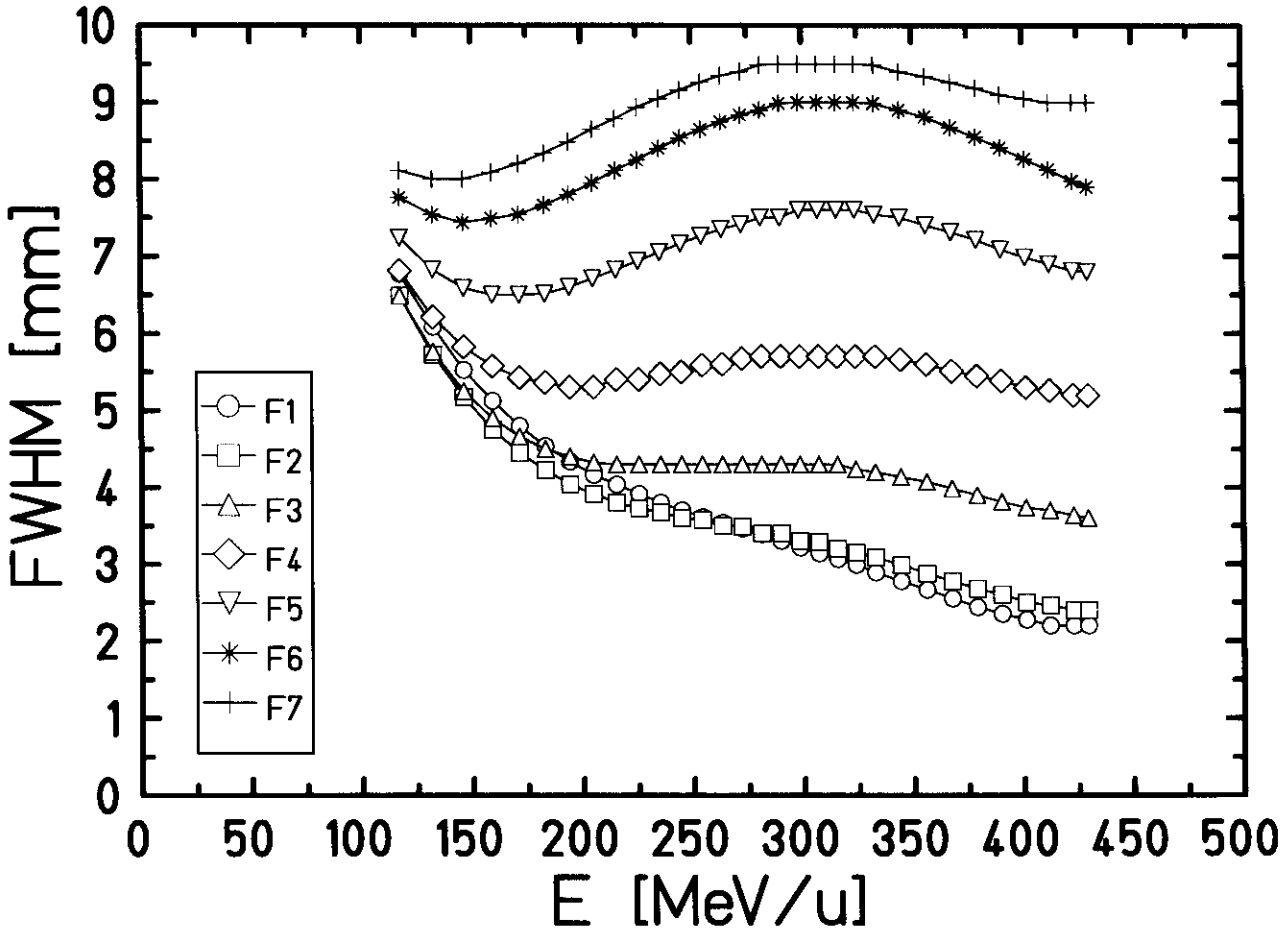


**Figure 3.** Dependence of the beam spot size at the isocentre on the beam energy.

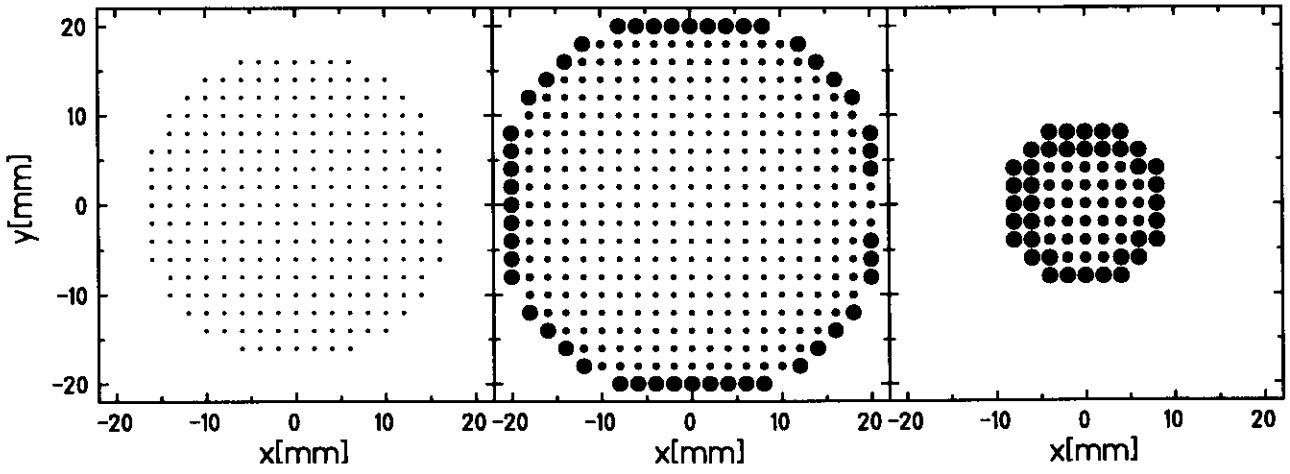


**Figure 4.** Particle fluence distributions corresponding to the energy slices indicated in figure 2.

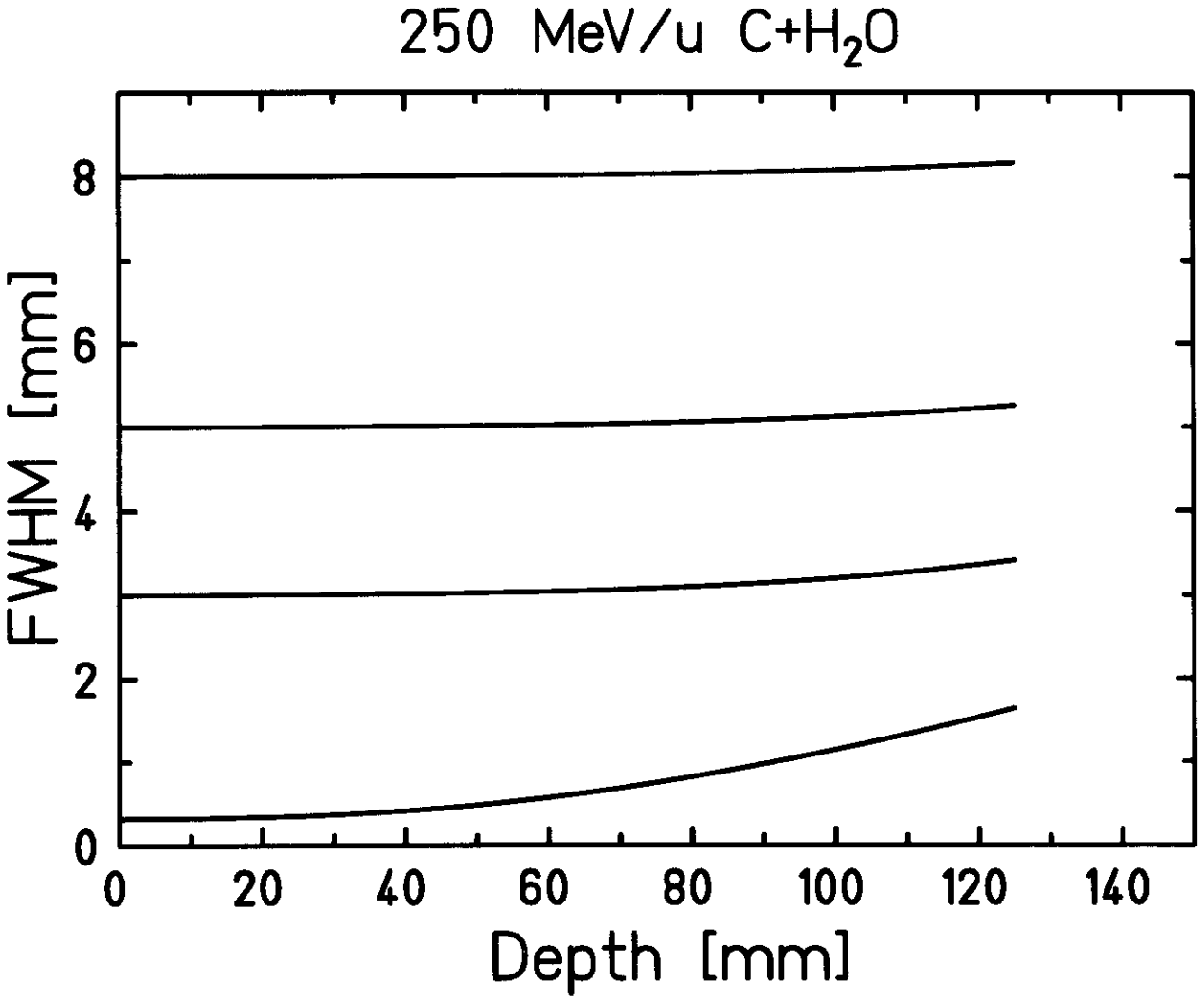


**Figure 5.** Lateral beam scattering in $H_2O$ calculated for a pure $^{12}C$ beam (nuclear fragmentation neglected) (Weber 1996). The width at depth zero is the initial beam width.

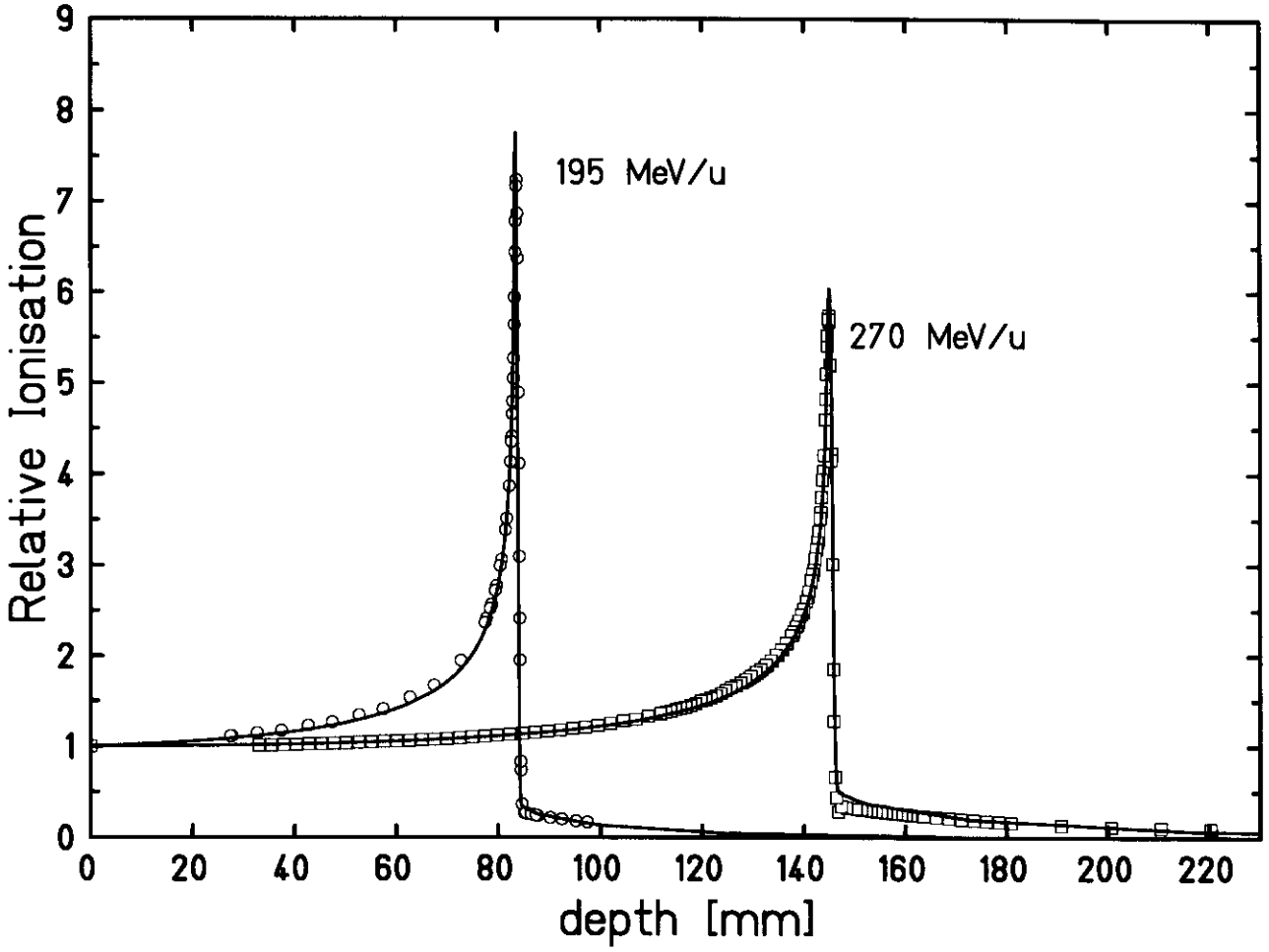


**Figure 6.** Measured (symbols) and calculated (lines) depth dose profiles for two typically used energies.

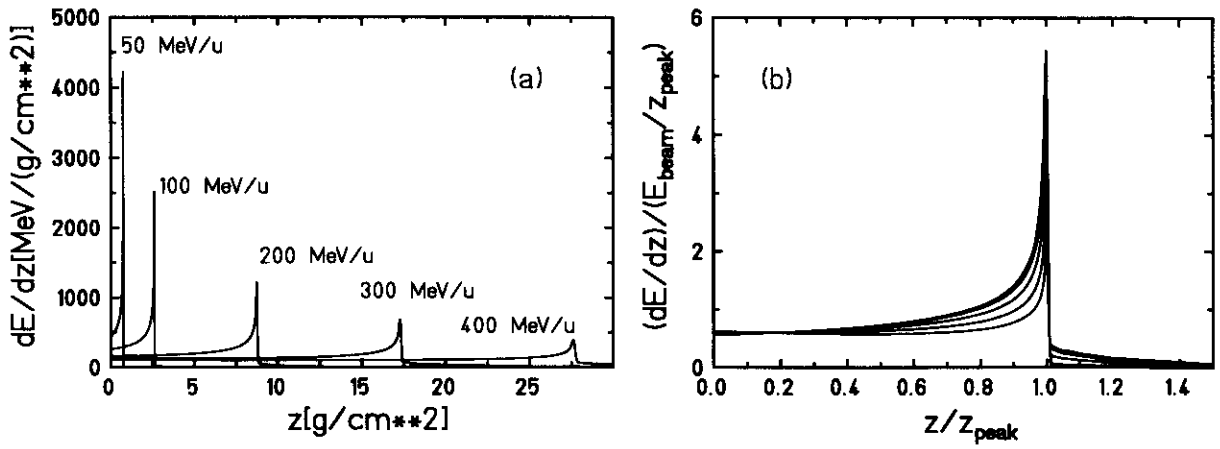


**Figure 7.** Interpolation of depth dose profiles. Original dose profiles for various beam energies (a) and profiles normalized to the Bragg peak position and the beam energy (b).

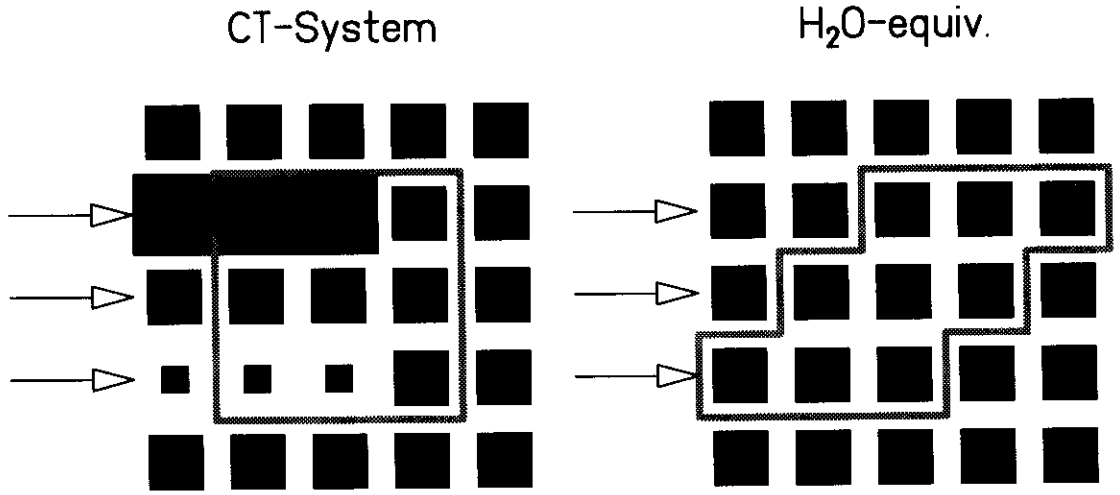


**Figure 8.** Transformation from CT- to waterequivalent system.

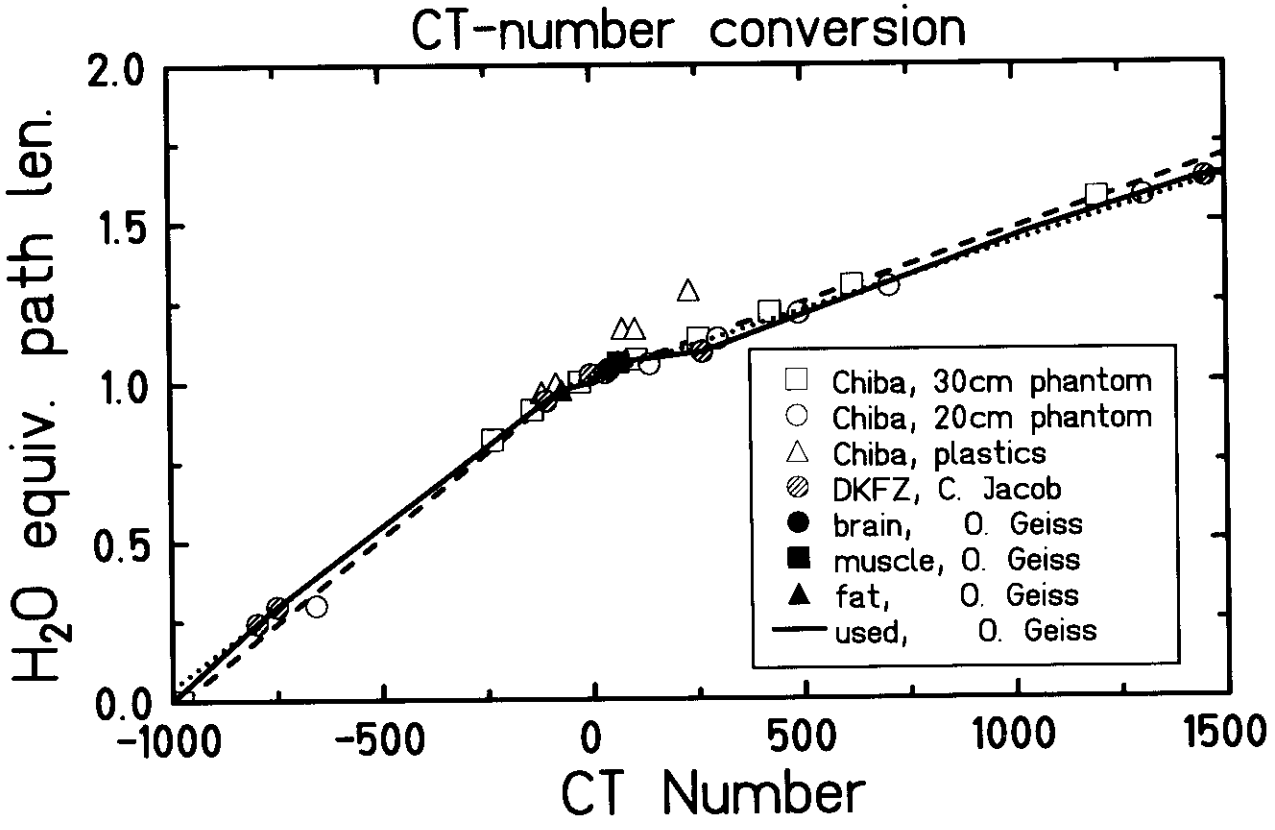


**Figure 9.** Correlation between CT Hounsfield numbers and water-equivalent path length. The dashed and dotted lines represent equations 6 and 7, respectively.

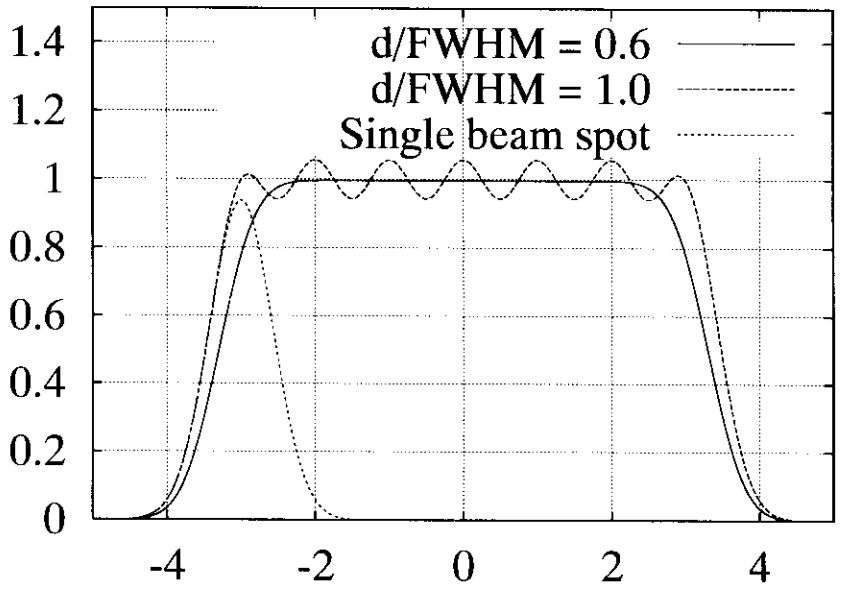


**Figure 10.** Homogeneity of lateral dose profile (solid and long-dashed lines) when using different fractions of the beam width as scanner step size (Weber 1996). The gaussian curve represents the profile of a single beam spot.

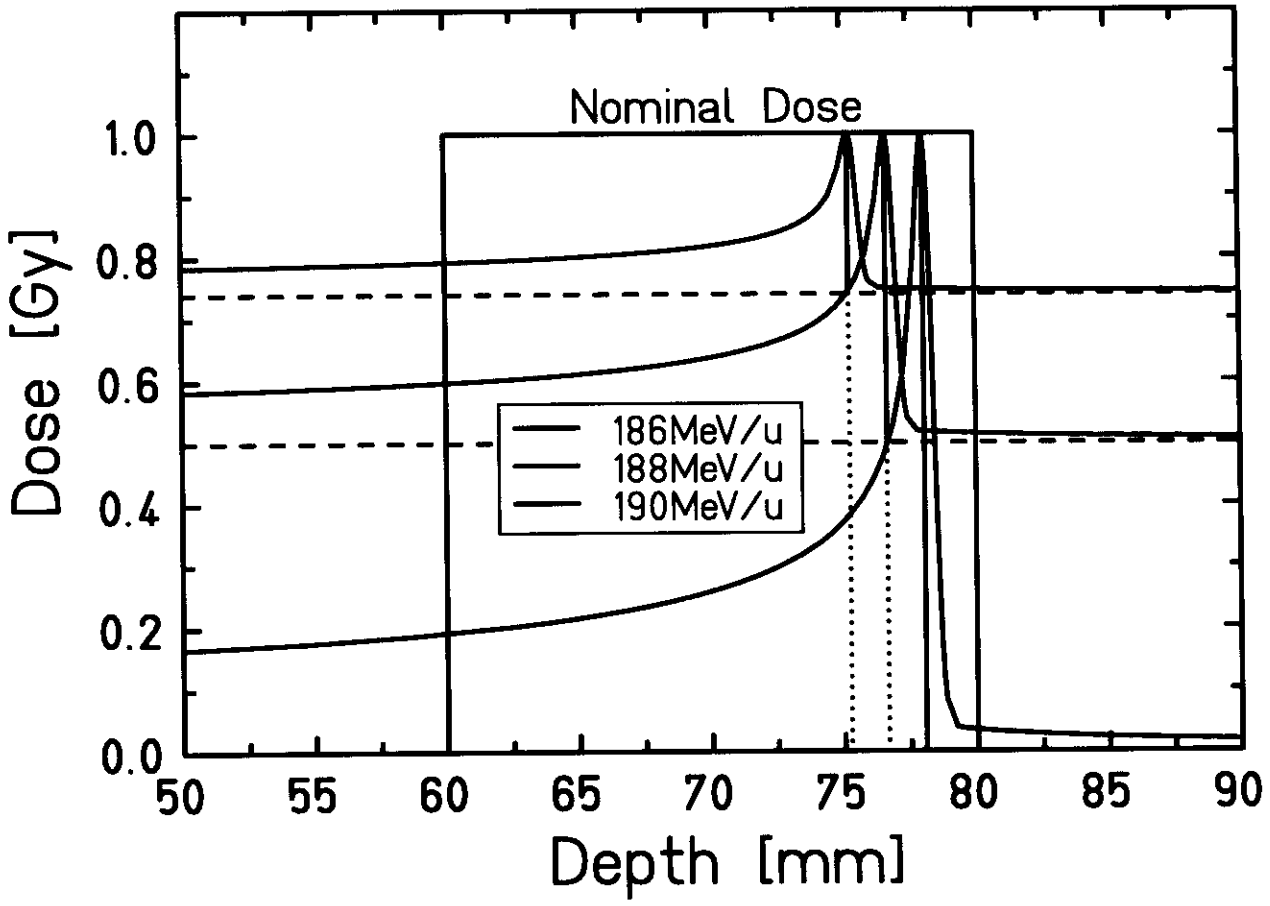


**Figure 11.** The principle of the first step of dose optimization. The dose contributions of lower beam energies are shifted on the ordinate to reflect the influence of preirradiation by higher beam energies.

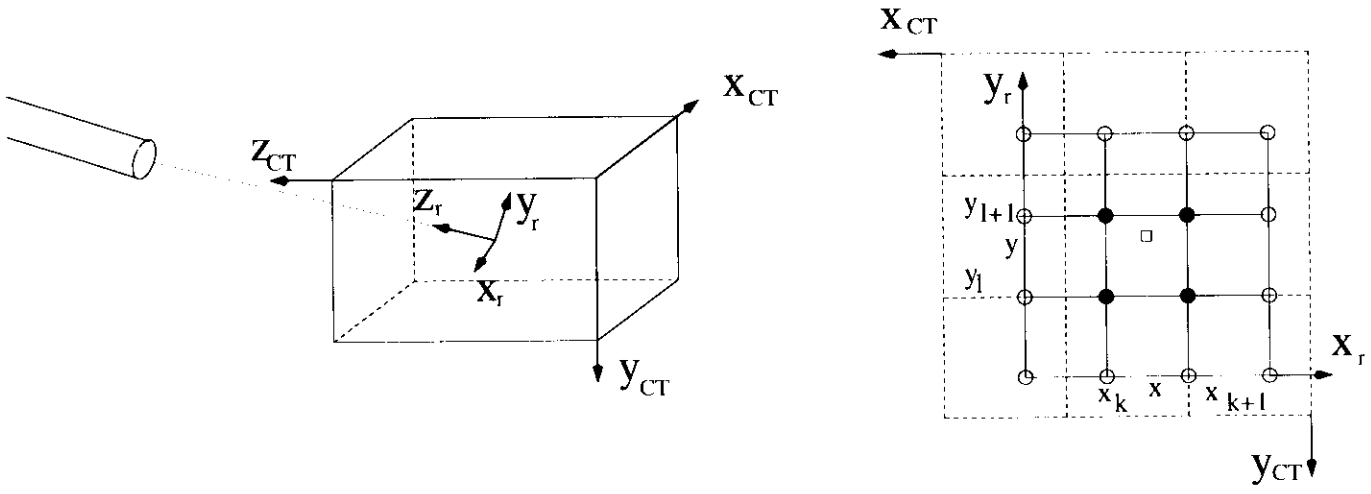


**Figure 12.** Relation between CT and raster coordinate system, equation 15

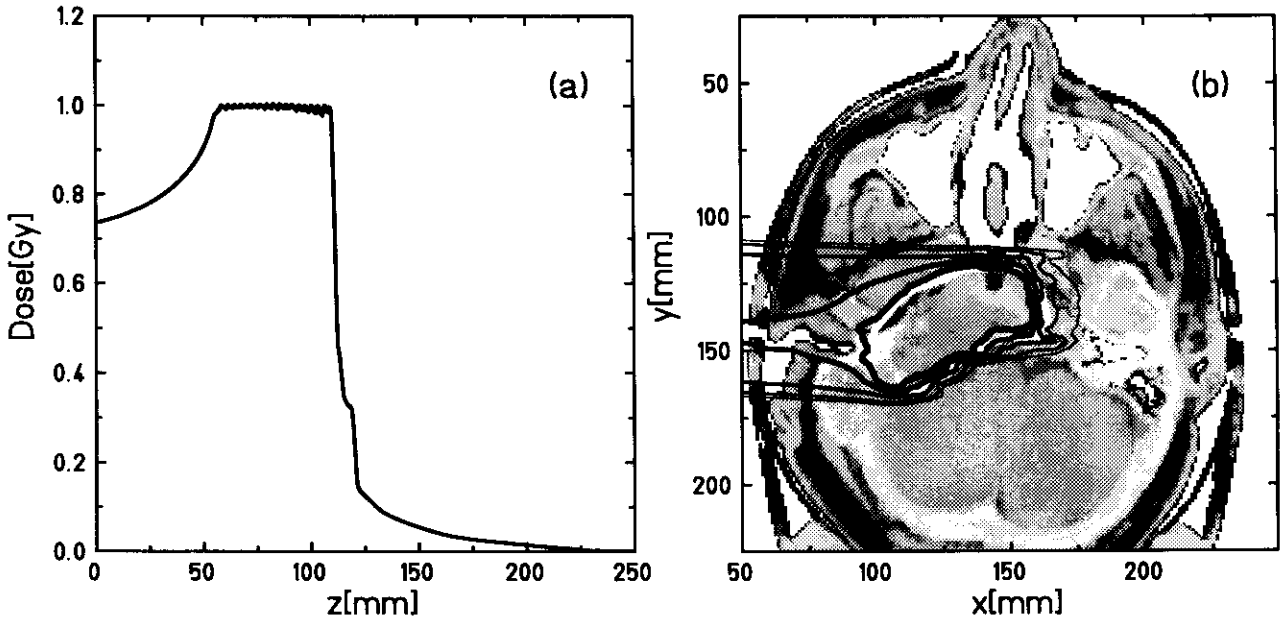


**Figure 13.** Calculated absorbed dose distribution for a patient after optimization. (a): In the water-equivalent system in beams-eye-view on a line through the isocentre. (b): Graphed on top of a CT image slice through the isocentre. The isodose lines correspond to 10, 20, 50, 80 and 95 percent.